

Photometric and Spectroscopic Observations of GRB 210104A: Bright Reverse shock Emission and Dense Circumburst Environment

LU-LU ZHANG,¹ LI-PING XIN*,² JING WANG,^{1,2} XU-HUI HAN,² DONG XU,² ZI-PEI ZHU,² CHAO WU,² JIAN-YAN WEI,² AND EN-WEI LIANG*¹

¹Guangxi Key Laboratory for Relativistic Astrophysics, School of Physical Science and Technology, Guangxi University, Nanning 530004, China

²Key Laboratory of Space Astronomy and Technology, National Astronomical Observatories, Chinese Academy of Sciences, Beijing 100101, China

ABSTRACT

Early afterglow observations of gamma-ray bursts (GRBs) are valuable for exploring the properties of their jets and ambient medium. We report our photometric and spectroscopic observations of GRB 210104A and discuss its jet properties with multiwavelength data. Our spectroscopic observation reveals several absorption features and a tentative redshift of 0.46 is identified. A bright optical flare that has a peak brightness of $R = 13$ mag at 112 ± 7 s was observed in the R band during $67 \sim 165$ seconds post the GRB trigger. The flux of the R -band afterglow decays with a slope of $\alpha_O = -0.91 \pm 0.03$ at $t > 650$ s. The early X-ray afterglow lightcurve is a smooth bump, and it decays with a slope of $\alpha_X = -1.18 \pm 0.01$ at late epoch. Our joint spectral fit to the optical-X-ray afterglows during $(1.1 - 1.3) \times 10^4$ s yields a photon index $\Gamma_{O,X} = -1.82 \pm 0.04$. The derived host galaxy extinction is $A_R = 0.87$. Attributing the early optical flare to the reverse-shock (RS) emission and the late optical-X-ray emission to the forward shock emission; the optical and X-ray lightcurves at $t < 3 \times 10^4$ s can be well fit adopting an Markov Chain Monte Carlo algorithm. Comparing the properties of GRB 210104A with other GRBs that have detection of bright RS emission, we show that its jet is mildly magnetized ($R_B = 28$), with high radiation efficiency (77%), is sub-energetic ($E_{k,iso} = 4.5 \times 10^{51}$ erg), and moderately relativistic ($\Gamma_0 \sim 35$) in a density medium ($n_0 \sim 417 \text{ cm}^{-3}$). It follows the tight $L_{\gamma,iso} - E_{p,z} - \Gamma_0$ relation as with typical GRBs.

Keywords: gamma-ray bursts (629); Interstellar dust extinction (837)

1. INTRODUCTION

Gamma-ray bursts (GRBs) and their afterglows are the most luminous transients in the universe. Their isotropic prompt gamma-ray energy is typically $10^{51} \sim 10^{54}$ erg, and their bright X-ray afterglows were detected with the X-Ray Telescope (XRT) for almost 90% of GRBs triggered with the Burst Alert Telescope (BAT) on board the Swift mission (e.g., Gehrels et al. 2009). Their optical afterglow can even be seen by eyes. The record holder so far is GRB 080319B, the so-called naked-eye GRB, which has an extremely bright optical afterglow with a peak visual magnitude of 5.3 at redshift of $z = 0.937$ (Racusin et al. 2008). Early bright optical flares were detected in some GRBs, such as GRB 990123 (~ 9 mag in the R band at $z = 1.6$; Akerlof et al. 1999), GRB 080129 (~ 17.5 mag in the J band at $z = 4.349 \pm 0.002$; Greiner et al. 2009), GRB 090102 (~ 13.4 in the R band at $z = 1.547$; Klotz et al. 2009; Mangano et al. 2009), GRB 130427A (7.03 ± 0.03 mag in the r' band at $z = 0.34$; Vestrand et al. 2014), and GRB 140512A (13 mag in the R band at $z = 0.725$; Huang et al. 2016). These flare-like optical afterglows are thought to be the external reverse-shock (RS) emission of the GRB jets (e.g., Mészáros & Rees 1999; Sari & Piran 1999a,b; Kobayashi & Sari 2000). They are powerful probes for investigating the physical properties of the radiating region and its surrounding medium (e.g., Sari & Piran 1999b; Kobayashi & Zhang 2003; Japelj et al. 2014; Gao et al. 2015; Yi et al. 2020).

Comparing to the onset peak of the forward shock (FS) emission, the optical flares produced by the RS are rarely detected. It was suggested that the RS emission could be suppressed by strong magnetization of the RS region (Zhang & Kobayashi 2005; Mimica et al. 2009; Mizuno et al. 2009) or the RS emission peaks at a lower energy band (Mundell et al. 2007; Melandri et al. 2010; Resmi & Zhang 2016). Alternately, the RS emission may also be masked by the prompt emission from the internal shocks (Kopač et al. 2013). RS emission is a critical probe to study the magnetization of the jet (e.g., Chen & Liu 2021). With detection of RS emission in some GRBs, it is found that the magnetization of the RS region is stronger than that in the FS region by a magnetization parameter of $R_B = \epsilon_B^r/\epsilon_B^f = 2 - 10^4$, where ϵ_B^f and ϵ_B^r are the magnetic equipartition parameters of the FS and RS regions (Zhang et al. 2003; Japelj et al. 2014). The RS emission could dominate the early optical afterglow emission if the typical value of $R_B \sim 100$ (Gao et al. 2015).

As a cosmic beacon, the GRB afterglows are probes for the ambient medium surrounding GRB jets (e.g., Levesque et al. 2010; Covino et al. 2013). The medium density surrounding a short GRBs, which are produced by the mergers of compact stars, is expected to be low (Panaitescu et al. 2001; Perna & Belczynski 2002; Xin et al. 2011). Long GRBs originate from the collapse of massive stars and they usually occur in the star formation region. It is found that long GRB host galaxies generally have a low-metallicity interstellar medium (ISM) environment (e.g., Fruchter et al. 2006). The medium density profile of some GRBs can be parameterized as $\rho \propto r^{-2}$, where r is the distance to the progenitor, implying the surrounding medium should be wind medium (e.g., Dai & Lu 1998; Mészáros et al. 1998; Panaitescu et al. 1998; Chevalier & Li 1999, 2000). By analyzing the temporal feature of the optical afterglow onset bumps for a sample of GRBs, it is found that the medium density profile at the early stage is $\rho \propto r^{-k}$ with a typical k value as 1 (e.g., Liang et al. 2013). Some unusual temporal features, such as a bump or the transition of a flux decaying slope, may also hint at the unique properties of the ambient density, e.g., a medium density jump or the transition of the medium profile, or the preheated and ionized medium (e.g., Dai & Lu 2002; Beloborodov 2005; Zhang et al. 2021).

This paper reports our photometric and spectroscopic observations of GRB 210104A with the GWAC-F60, 0.8 m TNT telescopes, and 2.16 m telescope at Xinglong observatory. A bright optical flare was observed in its very early optical afterglows. It is a valuable case for enlarging our GRB sample with detection of a very early optical flare for studying the GRB jet properties and ambient density. Our observations and data reduction is reported in § 2, and the data analysis is present in § 3. Discussion of our analysis results and implications for the GRB jet properties are reported in § 5. We summarize our results in § 6. Throughout, the convention $Q = 10^n Q_n$ in the cgs units and $F \propto t^\alpha \nu^\beta$ are adopted. We take the cosmology parameters as $H_0 = 67.8 \text{ km s}^{-1} \text{ Mpc}^{-1}$, and $\Omega_M = 0.308$ (Planck Collaboration et al. 2016).

2. OBSERVATIONS AND DATA REDUCTION

At 11:26:59.87 UT on 2021 January 4, the Fermi Gamma-Ray Burst Monitor (GBM) triggered and located GRB 210104A, which was also detected by Swift/BAT (Malacaria et al. 2021; Troja et al. 2021). The Fermi/GBM final real-time localization is consistent with the Swift position (Fermi GBM Team 2021). Its X-ray afterglows were detected with Swift/XRT since 62.7 s after the BAT trigger. We download the Swift/XRT lightcurve data from the website of Swift Burst Analyzer¹.

We carried out photometric follow-up observations by both GWAC-F60A² and 0.8 m TNT telescopes³ located at Xinglong observatory, National Astronomical Observatories of Chinese Academy of Sciences. The follow-ups were started by GWAC-F60A and 0.8 m TNT about 61 and 11246 s after the BAT trigger, respectively. Note that optical afterglow observation with the Swift/UVOT began at 71 s after the BAT trigger (Breeveld et al. 2021). Our optical detection is earlier than UVOT. The standard Johnson-Cousins B , R and I bands are used for GWAC-F60A, and the B and R bands for TNT. The exposure times range from 10 to 2100 s depending on the filters and the evolution of the brightness (Xin et al. 2021). Raw images taken by both telescopes were reduced by following the standard routine in the IRAF package, including bias, dark, flat-field corrections. The standard aperture photometry was adopted for building the lightcurves, in which the absolute calibration of the brightness was performed by using the Sloan Digital Sky Survey (SDSS) catalog (Adelman-McCarthy et al. 2008), with flux/mag conversion of the SDSS system into the Johnson-Cousins system⁴. Moreover, the r band was observed by using the NEXT-0.6 m optical telescope located at

¹ https://www.swift.ac.uk/xrt_curves/01015873/

² The GWAC-F60A telescope with a diameter of 60 cm is a follow-up facility belonging to the GWAC system.

³ TNT is a 0.8 m Tsinghua University - National Astronomical Observatory of China Telescope at Xinglong Observatory runs by a custom-designed automation system for GRB follow-up observations (Zheng et al. 2008). A PI 1300 × 1340 CCD and filters in the standard Johnson Bessel system are equipped for TNT.

⁴ <http://www.sdss.org/dr6/algorithms/sdssUBVRITransform.html#Lupton2005>

Nanshan, Xinjiang, China. Observations started at 11:59:19 UT and ended at 22:34:07 UT on 2021 January 4 (Zhu et al. 2021). The observation log and the resulting absolutely calibrated magnitudes of our photometric observations are listed in Table 1.

We carried out spectroscopic observations at 11:28:00 UT on 2021 Jan 4, about 1 hr after the burst trigger, with the 2.16 m telescope in Xinglong Observatory (Fan et al. 2016). The optical spectrum of afterglow of the burst was taken by the Beijing Faint Object Spectrograph and Camera (BFOSC) that is equipped with a back-illuminated E2V55-30 AIMO CCD. The grism G4 was used in the observation, which provides a wavelength coverage of 3600 – 8400 Å in the observer frame. A slit width of 1.8'' oriented in the south-north direction was adopted. The spectral resolution was resulted to be 10Å as measured from the sky lines. The exposure time is 3600 seconds. The wavelength calibration was carried out with the iron-argon comparison lamps, and the flux calibrations with the observations of the Kitt Peak National Observatory standard stars (Massey & Johnson 1998). The observed two-dimensional spectrum was reduced by the standard procedures, including bias subtraction and the flat-field correction using the IRAF package. The extracted one-dimensional spectrum was calibrated in wavelength and in flux by the corresponding comparison lamp and standards. The accuracy of the wavelength calibration is $\sim 1\text{\AA}$.

Figure 1 shows the extracted spectrum from our spectroscopic observations in the observer frame after smoothing by a box size of 3Å. Although the signal-to-noise ratio of the continuum is low, one can potentially identify a few absorption features due to Mg II $\lambda 2800$ and Fe II multiplets. This identification returns an estimation of redshift of $z = 0.46$.

3. DATA ANALYSIS

We convert the magnitude of the optical data to the cgs units with the zero-point flux of each band from Bessell et al. (1998). Note that the optical data are corrected for the extinction of our Galaxy with $R = 0.091$, $I = 0.063$, and $B = 0.151$ (Schlafly & Finkbeiner 2011). We show the optical and X-ray afterglow lightcurves in the left panel of Figure 2. We empirically fit the lightcurves with a single power-law function or a smooth broken power-law (BPL) function $F = F_0[(t/t_b)^{\alpha_1\omega} + (t/t_b)^{\alpha_2\omega}]^{1/\omega}$, where ω depicts the conjunction sharpness of the two segments. Note that the slopes derived from the smooth broken power-law model depend on ω , especially for a very smooth, broad bump like the X-ray afterglow lightcurve. We fix ω as 1 in our analysis. We adopt the least-square algorithm for our fit and evaluate the goodness with the reduced χ^2 .

Our results are shown in the left panel of Figure 2. The χ_r^2 of our best fit to the R -band lightcurve is 1.74. Our fit shows that the early R -band flare peaks at $t_{p,O} = 112 \pm 7$ s, and its rising and decaying slopes are $\alpha_{1,R} = 2.02 \pm 0.30$ and $\alpha_{2,R} = -2.07 \pm 0.14$, respectively. The slopes are similar to that usually seen in the early optical flares (e.g., Gao et al. 2015; Huang et al. 2016). The R -band lightcurve at $t > 10^3$ s is dominated by another smooth BPL component, and the decaying slope at the late epoch is $\alpha_{3,R} = -0.91 \pm 0.03$. The decaying phase of the early optical flare is also well observed in the I -band, but the rising part and the peak are missed. By rescaling the flux level, we found that the R -band lightcurve fit can apply to the I band lightcurve, i.e., $\alpha_{2,I} = -2.07$ and $\alpha_{3,I} = -0.91$, with $\chi^2 = 1.11$. The afterglows in the r and B bands are detected only at $t > 10^4$ seconds, and their decay slopes are $\alpha_{3,r} = -0.76 \pm 0.02$ ($\chi^2 = 2.95$) and $\alpha_{3,B} = -1.19 \pm 0.06$ ($\chi^2 = 0.67$).

The early X-ray afterglow lightcurve is completely different from the optical afterglow. Following an initial rapid decaying phase, the lightcurve shows a very smooth bump. The initial rapid decaying X-ray emission would be resulted from the prompt gamma-ray tail emission being due the curvature effect (e.g. Liang et al. 2006). Ignoring this component, our fit gives $\alpha_{1,X} \sim 1$, $\alpha_{2,X} = -1.18 \pm 0.01$, and $t_{p,X} = 313 \pm 6$ s by fixing $\omega = 1$. The χ_r^2 of the fit is 1.45.

We make a joint spectral analysis of the optical and X-ray data in the time interval from 1.1×10^4 to 1.3×10^4 s. Simultaneous observations in the X-ray, R , I , and B bands are available in this selected time interval. We extract the X-ray spectrum observed with Swift/XRT and adopt the XSPEC (version 12.12.1) package for making the spectral fit. Extinction and H I absorption of both our Galaxy and host galaxy are taken into account. The Galactic H I column density at the GRB direction is $N_{\text{H}}^{\text{Gal}} = 5.09 \times 10^{20} \text{ cm}^{-2}$. The extinction of our Galaxy in the GRB direction is $E(B - V) = 0.04$ (Schlegel et al. 1998). The extinction curve of the host galaxy is taken as the same as our Galaxy (Pei 1992) by setting $R_V = 3.08$. We find that an absorbed power-law model is equated to fit the spectrum and the derived photon index is $\Gamma_{O,X} = 1.82 \pm 0.04$. The reduced χ^2 is $39.34/40 = 0.98$. The hydrogen absorption of the host galaxy is $N_{\text{H}} = (6.22 \pm 2.31) \times 10^{20} \text{ cm}^{-2}$. The color index of the host galaxy is $E(B - V) = 0.36 \pm 0.06$, inferring an extinction in the R band of the host galaxy as $A_R = 0.87$ mag. This indicates that the burst environment is dusty.

4. THEORETICALLY MODELING OPTICAL AND X-RAY AFTERGLOW LIGHTCURVES

Our above analysis shows that the early optical flare seems to be attributed to the RS emission, and the late optical and X-ray emission should be the FS emission of the GRB fireball. It is uncertain whether the early X-ray bump can be explained with the external shock model. We fit the X-ray and optical lightcurves with the FS+RS afterglow model in this section. The details of our FS model are present in Sari et al. (1998), Huang et al. (2000), Fan & Piran (2006), and Ren et al. (2020). The RS model is referred to Yi et al. (2013) and Gao et al. (2015). The model parameters are the initial bulk Lorentz factor (Γ_0), the isotropic kinetic energy ($E_{k,\text{iso}}$), the medium number density (n_0), the energy partitions of the electrons (ϵ_e^f and ϵ_e^r) and magnetic fields (ϵ_B^f and ϵ_B^r) as well as the electron energy distribution power-law indices (p^f and p^r) of the FS and RS regions, where the superscripts “ f ” and “ r ” indicate the parameters of the FS and RS regions, respectively.

We fit the R -band and X-ray afterglow lightcurves with our model by adopting a Markov Chain Monte Carlo (MCMC) algorithm available in the Python package `emcee` (Foreman-Mackey et al. 2013). Note that the R -band lightcurve is corrected by the extinctions of both the host galaxy and our Galaxy. The probability contours of the model parameters derived from our fit are shown in Figure 4. The best fit yields the parameters and their 1σ uncertainty are: $\log_{10}\Gamma_0 = 1.55_{-0.02}^{+0.02}$, $\log_{10}E_{k,\text{iso}}(\text{erg}) = 51.65_{-0.02}^{+0.02}$, $\log_{10}n_0(\text{cm}^{-3}) = 2.62_{-0.15}^{+0.14}$, $\log_{10}\epsilon_e^f = -0.49_{-0.02}^{+0.02}$, $\log_{10}\epsilon_B^f = -3.90_{-0.13}^{+0.13}$, $p^f = 2.15_{-0.02}^{+0.02}$, $\log_{10}\epsilon_e^r = -0.84_{-0.05}^{+0.06}$, $\log_{10}\epsilon_B^r = -2.45_{-0.09}^{+0.10}$, and $p^r = 2.07_{-0.01}^{+0.01}$.

Our best fit is shown in Figure 3. It is found that the optical and X-ray afterglow lightcurves at $t < 3 \times 10^4$ s can be well fitted with our model. However, the model predicted X-ray flux at $t > 3 \times 10^4$ s is higher than the observed one. As shown in the left panel of Figure 2, the decay slope of the late X-ray afterglow index is $\alpha_{2,X} = 1.18 \pm 0.01$, convincingly ruling out the possibility that the discrepancy results from the jet break effect. Our joint spectral analysis for the optical-X-ray afterglows around 10^4 s suggests that the X-ray and optical afterglows are in the same spectral regime, as shown in the right panel of Figure 2. It is possible that the late X-ray and optical afterglows are in different spectral regimes. α_X is steeper than that of the R -band afterglow ($\alpha_{3,R} = -0.91 \pm 0.03$), with a difference of $\Delta\alpha = 0.27$. The flux decay slope of the synchrotron emission depends on the spectral regime (e.g., Sari et al. 1998; Zhang et al. 2006). In a constant-density medium, we have $\alpha = 3(p^f - 1)/4 = 0.86$ in the $\nu_m < \nu < \nu_c$ spectral regime and $\alpha = (3p^f - 2)/4 = 1.1$ in the $\nu > \nu_c$ spectral regime by taking $p^f = 2.15$. Thus, the late optical afterglow should be in the $\nu_m < \nu < \nu_c$ spectral regime and the X-ray afterglows are in the $\nu_X > \nu_c$ regime. Our best theoretical fit with the MCMC algorithm models the late X-ray and optical afterglows in the same spectral regimes since the late X-ray data are sparse and largely uncertain.

5. DISCUSSION

GRB 210104A is of interest with its bright early optical flash. As mentioned in § 1, bright RS optical emission only detected in several GRBs (e.g., Japelj et al. 2014; Gao et al. 2015, and references therein). The lack might be explained with the suppression by strong magnetization of the RS region (Zhang & Kobayashi 2005; Mimica et al. 2009; Mizuno et al. 2009), the RS emission peak at a lower frequency than the optical band (Mundell et al. 2007; Melandri et al. 2010; Resmi & Zhang 2016), and/or masked by the prompt optical and forward shock emission components (Kopač et al. 2013). Different from the bright optical flash observed in GRB 090727 (Mundell et al. 2007), the optical flash of GRB 210104A is not associated with prompt gamma-ray and/or X-ray flare. It could not be originated from the internal shock. We attributed it to the RS emission of the GRB jet in our analysis. Detection of bright RS emission in the R band indicates that the typical frequency (ν_m^r) of the electron synchrotron emission in the RS region should be in the R band. We calculate the value of ν_m^r at the peak time of optical flash through $\nu_m^r = 3.3 \times 10^{12} [(p^r - 2)/(p^r - 1)]^2 (1+z)^{1/2} \epsilon_{B,-2}^r \epsilon_{e,-1}^r E_{k,52}^{1/2} t_{p,\text{day}}^{-3/2}$ (e.g., Sari et al. 1998; Yost et al. 2003). We obtain $\nu_m^r(t_p) = 2.86 \times 10^{14}$ Hz, which is closed to the R band (4.28×10^{14} Hz).

We compare the properties of GRB 210104A with a sample of GRBs available in Japelj et al. (2014). We derive the properties of GRB 210104A from the data observed with the GBM (8-1000 keV) on board the Fermi mission. Its duration is 32 s in the 50 – 300 keV band (Malacaria et al. 2021). We extract the GBM spectrum accumulated in the time interval from 1.5 to 33.5 s since the GBM trigger with the tool `gtburst`⁵. We use the data of two NaI detectors (na and nb) and one BGO detector (b1) based on the angle between each detector and the source. We fit the spectrum by using the Band function (Band et al. 1993) with the `XSPEC` package. We obtain a low-energy photon

⁵ The *Fermi*/GBM data are downloaded from the *Fermi* website <https://heasarc.gsfc.nasa.gov/FTP/fermi/data/gbm/triggers/2021/bn210104477/current/>.

index as -1.09 ± 0.06 , a high-energy photon index as -2.63 ± 0.35 , and a νf_ν spectrum peak energy $E_p = 199 \pm 34$ keV. The reduced χ^2 of the fit is 474/343. The derived $E_{\gamma,\text{iso}}$ in the $1 - 10^4$ keV band is $1.30_{-0.23}^{+0.20} \times 10^{52}$ erg, and its peak luminosity is 2.5×10^{51} erg s $^{-1}$. The prompt and afterglow emission properties, including Γ_0 , $E_{\gamma,\text{iso}}$, $L_{\gamma,\text{iso}}$, $E_{k,\text{iso}}$, and E_p of GRB 210104A together with other GRBs from [Japelj et al. \(2014\)](#)⁶ are summarized in Table 2. These properties are dramatically different from each other, and each parameter is in a broad range among these GRBs, i.e., $E_{\gamma,\text{iso},52} = 1.1 \sim 239$, $E_{k,\text{iso},52} = 0.39 \sim 816$, $L_{\gamma,\text{iso},52} = 0.25 \sim 27$, and $E_p = 47 \sim 1028$ keV. These results imply that these GRBs do not have any universal features of their prompt gamma-ray and afterglow emission. They are not distinct from typical GRBs.

Measuring the magnetization of the jet with $R_B \equiv \epsilon_B^r/\epsilon_B^f$ ⁷, we calculate the R_B values of GRB 210104A and other GRBs in Table 2. In addition, the radiation efficiency, which is defined as $\eta_\gamma \equiv E_{\gamma,\text{iso}}/(E_{\gamma,\text{iso}} + E_{k,\text{iso}})$, is also a key probe for the jet composition (e.g., [Zhang et al. 2007](#); [Wang et al. 2015](#)). We also calculate their gamma-ray radiation efficiencies. Our results are also reported in Table 2. One can observe that R_B and η_γ values are dramatically different among these GRBs, i.e. $R_B = 4 \sim 16540$ and $\eta_\gamma = 0.02 \sim 0.77$. The radiation efficiency of GRB 210104A is the largest one among these GRBs, i.e., $\eta_\gamma = 77\%$. The high radiation efficiency is consistent with the expectation of a magnetized jet (e.g., [Zhang et al. 2007](#); [Wang et al. 2015](#)). [Gao et al. \(2015\)](#) reported a typical R_B value of ~ 100 for a sample of GRBs with detection of RS optical emission. GRB 210104A has a relative low R_B value among these GRBs. Its R_B value is 28, indicating that its jet is only moderately magnetized.

The derived Γ_0 of GRB 210104A from our fit is 35, indicating that the jet is middle relativistic. We test whether such a Γ_0 value violates the lower limit derived from the pair production opacity constraint. The spectrum of GRB 2101014A can be fitted with the Band function. Its high-energy spectrum is $f(E) = f(E_c)(E/E_c)^\beta$ for $E > E_c$, where $E_c = (\alpha - \beta)E_{\text{peak}}/(2 + \alpha)$ and $f(E_c) = A \exp(\beta - \alpha)(E_c/100 \text{ keV})^\alpha$. The minimum bulk Lorentz factor for the detection of maximum photon with energy E_0 sets a lower limit of Γ_0 as (e.g., [Lithwick & Sari 2001](#); see also [Abdo et al. 2009](#))

$$\Gamma_{\min} = \left[\sigma_T \left(\frac{d_L(z)}{c\Delta t} \right)^2 E_c f(E_c) F(\beta) \right]^{\frac{1}{2(1-\beta)}} (1+z)^{\frac{\beta+1}{1-\beta}} \left(\frac{E_0 E_c}{m_e^2 c^4} \right)^{\frac{\beta+1}{2(\beta-1)}}, \quad (1)$$

where σ_T is the Thompson scattering area, c is speed of light, d_L is the luminosity distance, m_e is the electron mass, $F(\beta)$ is a dimensionless function $F(\beta) = 4/(1-\beta) \int_0^1 dy (1-y^2)^{-\beta-2} g(y)y$, where $g(y) = 3/16(1-y^2)\{(3-y^4) \ln[(1+y)/(1-y)] - 2y(2-y^2)\}$, and Δt is the minimum variation timescale of prompt emission, which is taken as a typical value of 0.1 s ([MacLachlan et al. 2013](#)). The Konus-Wind mission detected the highest photon energy up to 2 MeV from GRB 210104A ([Frederiks et al. 2021](#)). Thus, we have $\Gamma_{\min} = 33$. The Γ_0 value derived from our fit is close to Γ_{\min} , but still does not violate the pair production opacity constraint.

[Liang et al. \(2015\)](#) found a tight $L_{\gamma,\text{iso}} - E_{p,z} - \Gamma_0$ correlation, i.e., $L_{\gamma,\text{iso}}^r = 10^{45.62 \pm 0.35} \text{ erg s}^{-1} (E_{p,z}/\text{keV})^{1.34 \pm 0.14} \Gamma_0^{1.32 \pm 0.19}$, where $E_{p,z} = E_p(1+z)$. This relation combines the jet luminosity (or energy), the initial Lorentz factor, and the radiation spectrum. It significantly reduces the intrinsic scatters of the $L_{\gamma,\text{iso}} - E_{p,z}$ ([Liang et al. 2004](#); [Amati 2006](#)) and $L_{\gamma,\text{iso}} - \Gamma_0$ ([Liang et al. 2010](#); [Lü et al. 2012](#)) relations, resulting in a much tighter relations than the $L_{\gamma,\text{iso}} - E_{p,z}$ and $L_{\gamma,\text{iso}} - \Gamma_0$ relation. This relation, which combines the observed luminosity with the properties of the GRB central engine, the medium density, and the radiation physics, should be an intrinsic feature of GRB jets (see also [Huang et al. 2020](#)). We examine whether GRB 210104A and other GRBs in Table 2 satisfy the $L_{\gamma,\text{iso}} - E_{p,z} - \Gamma_0$ correlation. We calculate the $L_{p,\text{iso},52}^r$ values and show $L_{p,\text{iso},52}^r$ as a function of $L_{p,\text{iso},52}$ in Figure 5. It is found that these GRBs follow well this relation. The RS GRBs taken from [Japelj et al. \(2014\)](#) tend to locate at the high luminosity end of this relation, indicating that their prompt gamma-ray luminosities are averagely brighter than typical LGRBs. This would be due to the sample selection effect. GRB 210104A is a relatively low-luminosity, subenergetic GRB among the RS GRBs.

6. SUMMARY

We have reported our spectroscopic and photometric observations of GRB 210104A and present our analysis on its properties of the jet and ambient medium. Our results are summarized below.

⁶ GRBs 021004 and 060908 are not included in our comparison since they are detected with Swift/BAT only and no broadband observations are available for constraining its prompt gamma-ray spectrum.

⁷ R_B is defined as $R_B \equiv (\epsilon_B^r/\epsilon_B^f)^{1/2}$ in [Zhang et al. \(2003\)](#). Here we adopt the definition as $R_B \equiv \epsilon_B^r/\epsilon_B^f$.

- The afterglow spectrum obtained from our spectroscopic observations at about 1 hr after the burst trigger reveals several absorption line features due to absorptions by Mg II λ 2800 and Fe II, and the redshift is estimated as $z = 0.46$.
- A bright early optical flare is observed in the R band in the time interval $67 \sim 152$ s post the GRB trigger. The flash has a peak brightness of $R = 13$ mag at 112 ± 7 s. The slope of the R -band afterglow lightcurve is $\alpha_{3,R} = -0.91 \pm 0.03$ at $t > 650$ s. The X-ray afterglow lightcurve features as a smooth onset bump at the early epoch and decays with a slope of $\alpha_{2,X} = -1.18 \pm 0.01$. Our joint optical-X-ray spectral analysis in the time slice of $t \in; [1.1, 1.3] \times 10^4$ s shows that a power-law with a photon index of $\Gamma_{O,X} = 1.82 \pm 0.04$ is equated to fit the spectrum. The derived H I absorption and dust extinction of the host galaxy are $N_H = 6.22_{-2.31}^{+2.31} \times 10^{20}$ cm $^{-2}$ and $A_R = 0.87$ mag by adopting an extinction curve as our Galaxy.
- The R -band and X-ray afterglow lightcurves of GRB 210104A at $t < 3 \times 10^4$ s can be fitted with the standard RS and FS models by adopting an MCMC algorithm. The early bright optical flare is attributed to the RS emission of the jet. The best fit yields the parameters and their 1σ uncertainties are: $\log_{10}\Gamma_0 = 1.55_{-0.02}^{+0.02}$, $\log_{10}E_{k,iso}(\text{erg}) = 51.65_{-0.02}^{+0.02}$, $\log_{10}n_0(\text{cm}^{-3}) = 2.62_{-0.15}^{+0.14}$, $\log_{10}\epsilon_e^f = -0.49_{-0.02}^{+0.02}$, $\log_{10}\epsilon_B^f = -3.90_{-0.13}^{+0.13}$, $p^f = 2.15_{-0.02}^{+0.02}$, $\log_{10}\epsilon_e^r = -0.84_{-0.05}^{+0.06}$, $\log_{10}\epsilon_B^r = -2.45_{-0.09}^{+0.10}$, and $p^r = 2.07_{-0.01}^{+0.01}$. The derived ν_m^r is very closed to the R band. Our theoretical analysis shows that the RS region is mildly magnetized ($R_B = 28$), suggesting that the jet is only moderately magnetized. The gamma-ray radiating efficiency is 77%. The jet is moderately relativistic ($\Gamma_0 = 35$). Such a low Γ_0 value does not violate the the lower limit derived from the pair production opacity constraint ($\Gamma_{\min} = 33$).
- We compare the properties of GRB 210104A with a sample of GRBs whose RS emission is detected in their early optical afterglows from [Japelj et al. \(2014\)](#). We do not find any universal features of their prompt gamma-ray and forward shock emission. They are not distinct from typical GRBs. They follow the $L_{\gamma,iso} - E_{p,z} - \Gamma_0$ relation derived from typical GRBs.

ACKNOWLEDGMENTS

We would like to thank the referee for a constructive report and thank Jia Ren for helpful discussions. We acknowledge the use of the public data from the Swift data archive and the UK Swift Science Data Center. This work is supported by the National Natural Science Foundation of China (grant Nos. 12133003, 11851304, and U1731239, 11973055, U1831207, 11863007, U1931133, U1938201). We acknowledge the support of the staff of the Xinglong 2.16 m telescope. This work was partially supported by the Open Project Program of the Key Laboratory of Optical Astronomy, National Astronomical Observatories, Chinese Academy of Sciences.

Facilities: GWAC-F60A and NAOC 2.16m optical telescopes at Xinglong Observatory, Heibei, China; NEXT-0.6m optical telescope located at Nanshan, Xinjiang, China

Software: IRAF ([Tody 1986](#); [Tody & Davis 1992](#)), emcee([Foreman-Mackey et al. 2013](#))

REFERENCES

- Abdo, A. A., Ackermann, M., Arimoto, M., et al. 2009, *Science*, 323, 1688, doi: [10.1126/science.1169101](https://doi.org/10.1126/science.1169101)
- Adelman-McCarthy, J. K., Agüeros, M. A., Allam, S. S., et al. 2008, *ApJS*, 175, 297, doi: [10.1086/524984](https://doi.org/10.1086/524984)
- Akerlof, C., Balsano, R., Barthelmy, S., et al. 1999, *Nature*, 398, 400, doi: [10.1038/18837](https://doi.org/10.1038/18837)
- Amati, L. 2006, *MNRAS*, 372, 233, doi: [10.1111/j.1365-2966.2006.10840.x](https://doi.org/10.1111/j.1365-2966.2006.10840.x)
- Band, D., Matteson, J., Ford, L., et al. 1993, *ApJ*, 413, 281, doi: [10.1086/172995](https://doi.org/10.1086/172995)
- Bellm, E., Bandstra, M., Boggs, S., et al. 2006, GRB Coordinates Network, 5867, 1
- Beloborodov, A. M. 2005, *ApJ*, 627, 346, doi: [10.1086/430166p](https://doi.org/10.1086/430166p)
- Bessell, M. S., Castelli, F., & Plez, B. 1998, *A&A*, 333, 231
- Breeveld, A. A., Troja, E., & Swift/UVOT Team. 2021, GRB Coordinates Network, 29247, 1
- Briggs, M. S., Band, D. L., Kippen, R. M., et al. 1999, *ApJ*, 524, 82, doi: [10.1086/307808](https://doi.org/10.1086/307808)
- Chen, Q., & Liu, X.-W. 2021, *MNRAS*, 504, 1759, doi: [10.1093/mnras/stab946](https://doi.org/10.1093/mnras/stab946)
- Chevalier, R. A., & Li, Z.-Y. 1999, *ApJL*, 520, L29, doi: [10.1086/312147](https://doi.org/10.1086/312147)
- . 2000, *ApJ*, 536, 195, doi: [10.1086/308914](https://doi.org/10.1086/308914)
- Covino, S., Melandri, A., Salvaterra, R., et al. 2013, *MNRAS*, 432, 1231, doi: [10.1093/mnras/stt540](https://doi.org/10.1093/mnras/stt540)
- Dai, Z. G. & Lu, T. 2002, *ApJL*, 565, L87, doi: [10.1086/339418p](https://doi.org/10.1086/339418p)
- Dai, Z. G., & Lu, T. 1998, *MNRAS*, 298, 87, doi: [10.1046/j.1365-8711.1998.01681.x](https://doi.org/10.1046/j.1365-8711.1998.01681.x)
- Fan, Y., & Piran, T. 2006, *MNRAS*, 369, 197, doi: [10.1111/j.1365-2966.2006.10280.x](https://doi.org/10.1111/j.1365-2966.2006.10280.x)
- Fan, Z., Wang, H., Jiang, X., et al. 2016, *PASP*, 128, 115005, doi: [10.1088/1538-3873/128/969/115005](https://doi.org/10.1088/1538-3873/128/969/115005)
- Fermi GBM Team. 2021, GRB Coordinates Network, 29232, 1
- Foreman-Mackey, D., Hogg, D. W., Lang, D., & Goodman, J. 2013, *PASP*, 125, 306, doi: [10.1086/670067](https://doi.org/10.1086/670067)
- Frederiks, D., Golenetskii, S., Lysenko, A., et al. 2021, GRB Coordinates Network, 29258, 1
- Fruchter, A. S., Levan, A. J., Strolger, L., et al. 2006, *Nature*, 441, 463, doi: [10.1038/nature04787](https://doi.org/10.1038/nature04787)
- Gao, H., Wang, X.-G., Mészáros, P., & Zhang, B. 2015, *ApJ*, 810, 160, doi: [10.1088/0004-637X/810/2/160](https://doi.org/10.1088/0004-637X/810/2/160)
- Gehrels, N., Ramirez-Ruiz, E., & Fox, D. B. 2009, *ARA&A*, 47, 567, doi: [10.1146/annurev.astro.46.060407.145147](https://doi.org/10.1146/annurev.astro.46.060407.145147)
- Golenetskii, S., Aptekar, R., Mazets, E., et al. 2009, GRB Coordinates Network, 8776, 1
- Greiner, J., Krühler, T., McBreen, S., et al. 2009, *ApJ*, 693, 1912, doi: [10.1088/0004-637X/693/2/1912](https://doi.org/10.1088/0004-637X/693/2/1912)
- Guidorzi, C., Frontera, F., Montanari, E., et al. 2005, *MNRAS*, 363, 315, doi: [10.1111/j.1365-2966.2005.09450.x](https://doi.org/10.1111/j.1365-2966.2005.09450.x)
- Huang, X.-L., Liang, E.-W., Liu, R.-Y., Cheng, J.-G., & Wang, X.-Y. 2020, *ApJL*, 903, L26, doi: [10.3847/2041-8213/abc330](https://doi.org/10.3847/2041-8213/abc330)
- Huang, X.-L., Xin, L.-P., Yi, S.-X., et al. 2016, *ApJ*, 833, 100, doi: [10.3847/1538-4357/833/1/100](https://doi.org/10.3847/1538-4357/833/1/100)
- Huang, Y. F., Gou, L. J., Dai, Z. G., & Lu, T. 2000, *ApJ*, 543, 90, doi: [10.1086/317076](https://doi.org/10.1086/317076)
- Japelj, J., Kopač, D., Kobayashi, S., et al. 2014, *ApJ*, 785, 84, doi: [10.1088/0004-637X/785/2/84](https://doi.org/10.1088/0004-637X/785/2/84)
- Jin, Z.-P., Covino, S., Della Valle, M., et al. 2013, *ApJ*, 774, 114, doi: [10.1088/0004-637X/774/2/114](https://doi.org/10.1088/0004-637X/774/2/114)
- Klotz, A., Gendre, B., Boer, M., & Atteia, J. L. 2009, GRB Coordinates Network, 8764, 1
- Kobayashi, S., & Sari, R. 2000, *ApJ*, 542, 819, doi: [10.1086/317021](https://doi.org/10.1086/317021)
- Kobayashi, S., & Zhang, B. 2003, *ApJ*, 597, 455, doi: [10.1086/378283](https://doi.org/10.1086/378283)
- Kopač, D., Kobayashi, S., Gomboc, A., et al. 2013, *ApJ*, 772, 73, doi: [10.1088/0004-637X/772/1/73](https://doi.org/10.1088/0004-637X/772/1/73)
- Kumar, P., & Panaitescu, A. 2003, *MNRAS*, 346, 905, doi: [10.1111/j.1365-2966.2003.07138.x](https://doi.org/10.1111/j.1365-2966.2003.07138.x)
- Levesque, E. M., Berger, E., Kewley, L. J., et al. 2010, *AJ*, 139, 694, doi: [10.1088/0004-6256/139/2/694](https://doi.org/10.1088/0004-6256/139/2/694)
- Liang, E. W., Dai, Z. G., & Wu, X. F. 2004, *ApJL*, 606, L29, doi: [10.1086/421047](https://doi.org/10.1086/421047)
- Liang, E. W., Zhang, B., O'Brien, P. T., et al. 2006, *ApJ*, 646, 351, doi: [10.1086/504684](https://doi.org/10.1086/504684)
- Liang, E.-W., Lin, T.-T., Lü, J., et al. 2015, *ApJ*, 813, 116, doi: [10.1088/0004-637X/813/2/116](https://doi.org/10.1088/0004-637X/813/2/116)
- Liang, E.-W., Yi, S.-X., Zhang, J., et al. 2010, *ApJ*, 725, 2209, doi: [10.1088/0004-637X/725/2/2209](https://doi.org/10.1088/0004-637X/725/2/2209)
- Liang, E.-W., Li, L., Gao, H., et al. 2013, *ApJ*, 774, 13, doi: [10.1088/0004-637X/774/1/13](https://doi.org/10.1088/0004-637X/774/1/13)
- Lithwick, Y., & Sari, R. 2001, *ApJ*, 555, 540, doi: [10.1086/321455](https://doi.org/10.1086/321455)
- Lü, J., Zou, Y.-C., Lei, W.-H., et al. 2012, *ApJ*, 751, 49, doi: [10.1088/0004-637X/751/1/49](https://doi.org/10.1088/0004-637X/751/1/49)
- MacLachlan, G. A., Shenoy, A., Sonbas, E., et al. 2013, *MNRAS*, 432, 857, doi: [10.1093/mnras/stt241](https://doi.org/10.1093/mnras/stt241)
- Malacaria, C., Fletcher, C., Meegan, C., & Fermi GBM Team. 2021, GRB Coordinates Network, 29246, 1
- Mangano, V., La Parola, V., & Sbarufatti, B. 2009, GRB Coordinates Network, 8767, 1
- Massey, P., & Johnson, O. 1998, *ApJ*, 505, 793, doi: [10.1086/306199](https://doi.org/10.1086/306199)

- Melandri, A., Kobayashi, S., Mundell, C. G., et al. 2010, *ApJ*, 723, 1331, doi: [10.1088/0004-637X/723/2/1331](https://doi.org/10.1088/0004-637X/723/2/1331)
- Mészáros, P., & Rees, M. J. 1999, *MNRAS*, 306, L39, doi: [10.1046/j.1365-8711.1999.02800.x](https://doi.org/10.1046/j.1365-8711.1999.02800.x)
- Mészáros, P., Rees, M. J., & Wijers, R. A. M. J. 1998, *ApJ*, 499, 301, doi: [10.1086/305635](https://doi.org/10.1086/305635)
- Mimica, P., Giannios, D., & Aloy, M. A. 2009, *A&A*, 494, 879, doi: [10.1051/0004-6361:200810756](https://doi.org/10.1051/0004-6361:200810756)
- Mizuno, Y., Zhang, B., Giacomazzo, B., et al. 2009, *ApJL*, 690, L47, doi: [10.1088/0004-637X/690/1/L47](https://doi.org/10.1088/0004-637X/690/1/L47)
- Mundell, C. G., Steele, I. A., Smith, R. J., et al. 2007, *Science*, 315, 1822, doi: [10.1126/science.1138484](https://doi.org/10.1126/science.1138484)
- Panaitescu, A., Kumar, P., & Narayan, R. 2001, *ApJL*, 561, L171, doi: [10.1086/324678](https://doi.org/10.1086/324678)
- Panaitescu, A., Mészáros, P., & Rees, M. J. 1998, *ApJ*, 503, 314, doi: [10.1086/305995](https://doi.org/10.1086/305995)
- Pei, Y. C. 1992, *ApJ*, 395, 130, doi: [10.1086/171637](https://doi.org/10.1086/171637)
- Perna, R., & Belczynski, K. 2002, *ApJ*, 570, 252, doi: [10.1086/339571](https://doi.org/10.1086/339571)
- Planck Collaboration, Ade, P. A. R., Aghanim, N., et al. 2016, *A&A*, 594, A13, doi: [10.1051/0004-6361/201525830](https://doi.org/10.1051/0004-6361/201525830)
- Racusin, J. L., Karpov, S. V., Sokolowski, M., et al. 2008, *Nature*, 455, 183, doi: [10.1038/nature07270](https://doi.org/10.1038/nature07270)
- Ren, J., Lin, D.-B., Zhang, L.-L., et al. 2020, *ApJL*, 901, L26, doi: [10.3847/2041-8213/abb672](https://doi.org/10.3847/2041-8213/abb672)
- Resmi, L., & Zhang, B. 2016, *ApJ*, 825, 48, doi: [10.3847/0004-637X/825/1/48](https://doi.org/10.3847/0004-637X/825/1/48)
- Sari, R., & Piran, T. 1999a, *ApJ*, 520, 641, doi: [10.1086/307508](https://doi.org/10.1086/307508)
- . 1999b, *ApJL*, 517, L109, doi: [10.1086/312039](https://doi.org/10.1086/312039)
- Sari, R., Piran, T., & Narayan, R. 1998, *ApJL*, 497, L17, doi: [10.1086/311269](https://doi.org/10.1086/311269)
- Schlaflly, E., & Finkbeiner, D. P. 2011, *ApJ*, 737, 103, doi: [10.1088/0004-637X/737/2/103](https://doi.org/10.1088/0004-637X/737/2/103)
- Schlegel, D. J., Finkbeiner, D. P., & Davis, M. 1998, *ApJ*, 500, 525, doi: [10.1086/305772](https://doi.org/10.1086/305772)
- Tody, D. 1986, in *Society of Photo-Optical Instrumentation Engineers (SPIE) Conference Series*, Vol. 627, *Instrumentation in astronomy VI*, ed. D. L. Crawford, 733, doi: [10.1117/12.968154](https://doi.org/10.1117/12.968154)
- Tody, D., & Davis, L. E. 1992, in *Astronomical Society of the Pacific Conference Series*, Vol. 25, *Astronomical Data Analysis Software and Systems I*, ed. D. M. Worrall, C. Biemesderfer, & J. Barnes, 484
- Troja, E., Bernardini, M. G., Breeveld, A. A., et al. 2021, *GRB Coordinates Network*, 29233, 1
- Ukwatta, T. N., Stamatikos, M., Dhuga, K. S., et al. 2010, *ApJ*, 711, 1073, doi: [10.1088/0004-637X/711/2/1073](https://doi.org/10.1088/0004-637X/711/2/1073)
- Vestrand, W. T., Wren, J. A., Panaitescu, A., et al. 2014, *Science*, 343, 38, doi: [10.1126/science.1242316](https://doi.org/10.1126/science.1242316)
- Wang, X.-G., Zhang, B., Liang, E.-W., et al. 2015, *ApJS*, 219, 9, doi: [10.1088/0067-0049/219/1/9](https://doi.org/10.1088/0067-0049/219/1/9)
- Wei, D. M. 2003, *A&A*, 402, L9, doi: [10.1051/0004-6361:20030371](https://doi.org/10.1051/0004-6361:20030371)
- Xin, L.-P., Liang, E.-W., Wei, J.-Y., et al. 2011, *MNRAS*, 410, 27, doi: [10.1111/j.1365-2966.2010.17419.x](https://doi.org/10.1111/j.1365-2966.2010.17419.x)
- Xin, L. P., Wang, J., Han, X. H., et al. 2021, *GRB Coordinates Network*, 29235, 1
- Yi, S.-X., Wu, X.-F., & Dai, Z.-G. 2013, *ApJ*, 776, 120, doi: [10.1088/0004-637X/776/2/120](https://doi.org/10.1088/0004-637X/776/2/120)
- Yi, S.-X., Wu, X.-F., Zou, Y.-C., & Dai, Z.-G. 2020, *ApJ*, 895, 94, doi: [10.3847/1538-4357/ab8a53](https://doi.org/10.3847/1538-4357/ab8a53)
- Yost, S. A., Harrison, F. A., Sari, R., & Frail, D. A. 2003, *ApJ*, 597, 459, doi: [10.1086/378288](https://doi.org/10.1086/378288)
- Zhang, B., Fan, Y. Z., Dyks, J., et al. 2006, *ApJ*, 642, 354, doi: [10.1086/500723](https://doi.org/10.1086/500723)
- Zhang, L.-L., Ren, J., Huang, X.-L., et al. 2021, *ApJ*, 917, 95, doi: [10.3847/1538-4357/ac0c7f](https://doi.org/10.3847/1538-4357/ac0c7f)
- Zhang, B., & Kobayashi, S. 2005, *ApJ*, 628, 315, doi: [10.1086/429787](https://doi.org/10.1086/429787)
- Zhang, B., Kobayashi, S., & Mészáros, P. 2003, *ApJ*, 595, 950, doi: [10.1086/377363](https://doi.org/10.1086/377363)
- Zhang, B., Liang, E., Page, K. L., et al. 2007, *ApJ*, 655, 989, doi: [10.1086/510110](https://doi.org/10.1086/510110)
- Zheng, W.-K., Deng, J.-S., Zhai, M., et al. 2008, *ChJA&A*, 8, 693, doi: [10.1088/1009-9271/8/6/08](https://doi.org/10.1088/1009-9271/8/6/08)
- Zhu, Z. P., Fu, S. Y., Liu, X., et al. 2021, *GRB Coordinates Network*, 29252, 1

Table 1. Optical Afterglow Photometry Log of GRB 210104A

$T - T_0$ (mid,sec)	Exposure (sec)	Mag	Merr	Filter	Telescope
67	10	14.14	0.03	<i>R</i>	F60A
79	10	14.08	0.02	<i>R</i>	F60A
91	10	13.93	0.03	<i>R</i>	F60A
103	10	13.78	0.02	<i>R</i>	F60A
116	10	13.89	0.02	<i>R</i>	F60A
128	10	13.92	0.03	<i>R</i>	F60A
140	10	14.01	0.03	<i>R</i>	F60A
152	10	14.00	0.03	<i>R</i>	F60A
656	50	16.02	0.03	<i>R</i>	F60A
708	50	16.14	0.05	<i>R</i>	F60A
760	50	16.25	0.04	<i>R</i>	F60A
813	50	16.22	0.04	<i>R</i>	F60A
865	50	16.28	0.04	<i>R</i>	F60A
917	50	16.35	0.05	<i>R</i>	F60A
969	50	16.50	0.05	<i>R</i>	F60A
1021	50	16.46	0.05	<i>R</i>	F60A
1073	50	16.48	0.06	<i>R</i>	F60A
1125	50	16.46	0.08	<i>R</i>	F60A
1950	100	17.04	0.04	<i>R</i>	F60A
2053	100	17.07	0.04	<i>R</i>	F60A
2155	100	17.12	0.05	<i>R</i>	F60A
2257	100	17.09	0.04	<i>R</i>	F60A
2359	100	17.27	0.05	<i>R</i>	F60A
2461	100	17.23	0.05	<i>R</i>	F60A
2681	100	17.27	0.05	<i>R</i>	F60A
2783	100	17.35	0.06	<i>R</i>	F60A
2885	100	17.29	0.06	<i>R</i>	F60A
3127	100	17.35	0.05	<i>R</i>	F60A
3229	100	17.47	0.06	<i>R</i>	F60A
3331	100	17.46	0.06	<i>R</i>	F60A
3433	100	17.50	0.05	<i>R</i>	F60A
3638	100	17.36	0.05	<i>R</i>	F60A
3740	100	17.44	0.06	<i>R</i>	F60A
6047	150	18.01	0.09	<i>R</i>	F60A
6199	150	17.88	0.07	<i>R</i>	F60A
6351	150	17.84	0.07	<i>R</i>	F60A
6504	150	17.90	0.08	<i>R</i>	F60A
6656	150	17.95	0.08	<i>R</i>	F60A
6938	150	18.16	0.09	<i>R</i>	F60A
7091	150	18.16	0.10	<i>R</i>	F60A
7243	150	18.01	0.08	<i>R</i>	F60A
7395	150	18.20	0.10	<i>R</i>	F60A
7547	150	18.02	0.09	<i>R</i>	F60A
7699	150	18.02	0.09	<i>R</i>	F60A
7851	150	18.11	0.09	<i>R</i>	F60A
8003	150	18.15	0.10	<i>R</i>	F60A
8156	150	17.99	0.08	<i>R</i>	F60A

(Table 1. continued)

8308	150	18.26	0.10	<i>R</i>	F60A
9316	150	18.30	0.10	<i>R</i>	F60A
9468	150	18.14	0.10	<i>R</i>	F60A
9620	150	18.22	0.10	<i>R</i>	F60A
9772	150	18.41	0.13	<i>R</i>	F60A
9924	150	18.28	0.10	<i>R</i>	F60A
11240	150	18.55	0.16	<i>R</i>	F60A
11392	150	18.55	0.14	<i>R</i>	F60A
11545	150	18.63	0.17	<i>R</i>	F60A
11697	150	18.70	0.18	<i>R</i>	F60A
11849	150	18.87	0.24	<i>R</i>	F60A
12070	250	18.68	0.16	<i>R</i>	F60A
12322	250	18.39	0.12	<i>R</i>	F60A
12574	250	18.46	0.13	<i>R</i>	F60A
12849	250	18.38	0.11	<i>R</i>	F60A
13102	250	18.88	0.17	<i>R</i>	F60A
13354	250	18.70	0.15	<i>R</i>	F60A
17026	300	19.14	0.20	<i>R</i>	F60A
17328	300	18.71	0.14	<i>R</i>	F60A
17630	300	18.86	0.17	<i>R</i>	F60A
18235	300	19.10	0.24	<i>R</i>	F60A
12451	200	18.56	0.10	<i>R</i>	TNT
14037	300	18.82	0.10	<i>R</i>	TNT
14353	300	18.81	0.11	<i>R</i>	TNT
16588	300	19.00	0.11	<i>R</i>	TNT
16905	300	18.94	0.11	<i>R</i>	TNT
19600	1200	18.96	0.07	<i>R</i>	TNT
24704	1200	19.04	0.08	<i>R</i>	TNT
237	30	14.15	0.02	<i>I</i>	F60A
269	30	14.39	0.03	<i>I</i>	F60A
301	30	14.56	0.09	<i>I</i>	F60A
334	30	14.69	0.04	<i>I</i>	F60A
366	30	14.91	0.09	<i>I</i>	F60A
398	30	14.94	0.04	<i>II</i>	F60A
430	30	15.04	0.06	<i>II</i>	F60A
462	30	15.20	0.05	<i>I</i>	F60A
494	30	15.26	0.07	<i>I</i>	F60A
526	30	15.42	0.10	<i>I</i>	F60A
1238	60	16.25	0.10	<i>I</i>	F60A
1300	60	16.22	0.08	<i>I</i>	F60A
1362	60	16.23	0.07	<i>I</i>	F60A
1424	60	16.32	0.09	<i>I</i>	F60A
1486	60	16.42	0.10	<i>I</i>	F60A
1549	60	16.45	0.10	<i>I</i>	F60A
1611	60	16.25	0.07	<i>I</i>	F60A
1673	60	16.42	0.09	<i>I</i>	F60A
1735	60	16.56	0.09	<i>I</i>	F60A
1797	60	16.39	0.08	<i>I</i>	F60A
3844	100	16.95	0.09	<i>I</i>	F60A

(Table 1. continued)

3946	100	16.86	0.08	<i>I</i>	F60A
4048	100	17.14	0.11	<i>I</i>	F60A
4150	100	17.13	0.11	<i>I</i>	F60A
4355	100	17.16	0.10	<i>I</i>	F60A
4457	100	17.20	0.11	<i>I</i>	F60A
4559	100	17.20	0.10	<i>I</i>	F60A
4661	100	17.53	0.17	<i>I</i>	F60A
4865	100	17.02	0.08	<i>I</i>	F60A
5587	60	17.20	0.15	<i>I</i>	F60A
5649	60	17.39	0.17	<i>I</i>	F60A
5711	60	17.39	0.18	<i>I</i>	F60A
5773	60	17.31	0.17	<i>I</i>	F60A
5835	60	17.00	0.13	<i>I</i>	F60A
8966	150	17.83	0.16	<i>I</i>	F60A
9118	150	17.73	0.12	<i>I</i>	F60A
10798	200	17.94	0.15	<i>I</i>	F60A
11001	200	17.82	0.14	<i>I</i>	F60A
13332	200	18.38	0.13	<i>I</i>	TNT
13549	200	18.48	0.13	<i>I</i>	TNT
13766	200	18.28	0.12	<i>I</i>	TNT
15633	300	18.39	0.10	<i>I</i>	TNT
15950	300	18.37	0.11	<i>I</i>	TNT
16267	300	18.59	0.13	<i>I</i>	TNT
5305	500	18.72	0.09	<i>B</i>	F60A
9047	1000	19.31	0.08	<i>B</i>	F60A
11246	200	19.91	0.17	<i>B</i>	TNT
11463	200	19.83	0.15	<i>B</i>	TNT
11794	200	19.73	0.17	<i>B</i>	TNT
12011	200	20.03	0.22	<i>B</i>	TNT
12529	800	19.83	0.08	<i>B</i>	TNT
14975	900	20.04	0.10	<i>B</i>	TNT
17527	900	20.16	0.13	<i>B</i>	TNT
20079	900	20.45	0.20	<i>B</i>	TNT
23230	1800	20.64	0.16	<i>B</i>	TNT
28932	2100	20.80	0.23	<i>B</i>	TNT
2678	...	17.20	0.04	<i>r</i>	NEXT
2902	...	17.35	0.03	<i>r</i>	NEXT
3128	...	17.36	0.04	<i>r</i>	NEXT
3351	...	17.45	0.04	<i>r</i>	NEXT
3572	...	17.49	0.04	<i>r</i>	NEXT
3794	...	17.59	0.03	<i>r</i>	NEXT
4019	...	17.62	0.04	<i>r</i>	NEXT
4243	...	17.54	0.05	<i>r</i>	NEXT
4465	...	17.61	0.04	<i>r</i>	NEXT
4692	...	17.72	0.04	<i>r</i>	NEXT
4923	...	17.76	0.03	<i>r</i>	NEXT
5146	...	17.73	0.04	<i>r</i>	NEXT
5367	...	17.63	0.04	<i>r</i>	NEXT
5591	...	17.94	0.04	<i>r</i>	NEXT

(Table 1. continued)

5815	...	17.81	0.04	<i>r</i>	NEXT
6039	...	17.87	0.05	<i>r</i>	NEXT
6261	...	17.81	0.05	<i>r</i>	NEXT
6484	...	17.87	0.04	<i>r</i>	NEXT
6707	...	17.96	0.04	<i>r</i>	NEXT
6929	...	17.95	0.05	<i>r</i>	NEXT
7272	...	18.17	0.04	<i>r</i>	NEXT
7594	...	17.96	0.05	<i>r</i>	NEXT
7918	...	18.06	0.04	<i>r</i>	NEXT
8241	...	18.15	0.05	<i>r</i>	NEXT
8563	...	18.16	0.05	<i>r</i>	NEXT
8885	...	18.22	0.05	<i>r</i>	NEXT
9209	...	18.30	0.05	<i>r</i>	NEXT
9532	...	18.24	0.05	<i>r</i>	NEXT
9854	...	18.27	0.05	<i>r</i>	NEXT
10843	...	18.30	0.05	<i>r</i>	NEXT
11170	...	18.44	0.05	<i>r</i>	NEXT
11493	...	18.51	0.05	<i>r</i>	NEXT
11816	...	18.58	0.05	<i>r</i>	NEXT
12140	...	18.61	0.05	<i>r</i>	NEXT
12463	...	18.44	0.05	<i>r</i>	NEXT
12786	...	18.42	0.05	<i>r</i>	NEXT
38520	...	19.52	0.07	<i>r</i>	NEXT

Table 2. Prompt and afterglow emission properties of GRB 210104A in comparison with others GRBs with RS emission detection available in [Japelj et al. \(2014\)](#)

GRBs	z	Γ_0	$E_{\gamma,\text{iso}}$ (10^{52} erg)	$E_{k,\text{iso}}$ (10^{52} erg)	R_B	η_γ	E_p (keV)	$L_{\gamma,\text{iso}}$ (10^{52} erg s $^{-1}$)	References ^a
210104A	0.46	35	$1.30^{+0.20}_{-0.23}$	0.39	28	0.77	199^{+34}_{-34}	$0.25^{+0.11}_{-0.20}$	<i>This work</i>
990123	1.6	420	239 ± 28	108	1156	0.69	720^{+10}_{-10}	$8.40^{+1.21}_{-1.21}$	(1)
021211	1.006	154	1.10 ± 0.13	3	128	0.27	47^{+9}_{-7}	0.25	(2)
061126	1.1588	255	30 ± 3	12	69	0.71	935^{+360}_{-360}	2.28	(3)
080319B	0.9382	286	142 ± 3	67.6	16540	0.68	675^{+22}_{-22}	$10.1^{+0.9}_{-0.9}$	(4)
090102	1.547	228	21.4 ± 0.4	816	6666	0.03	451^{+73}_{-58}	7.8	(5)
090424	0.544	235	3.97 ± 0.08	258	25	0.02	236^{+127}_{-49}	$1.62^{+0.05}_{-0.04}$	(6)
130427A	0.34	157	85.0	521	4	0.14	1028^{+8}_{-8}	27.0	(7)

^aReferences for E_p and $L_{\gamma,\text{iso}}$: (1) [Briggs et al. \(1999\)](#), [Guidorzi et al. \(2005\)](#); (2) [Kumar & Panaitescu \(2003\)](#), [Wei \(2003\)](#); (3) [Bellm et al. \(2006\)](#); (4) [Racusin et al. \(2008\)](#); (5) [Golenetskii et al. \(2009\)](#); (6) [Ukwatta et al. \(2010\)](#), [Jin et al. \(2013\)](#); (7) [Huang et al. \(2020\)](#).

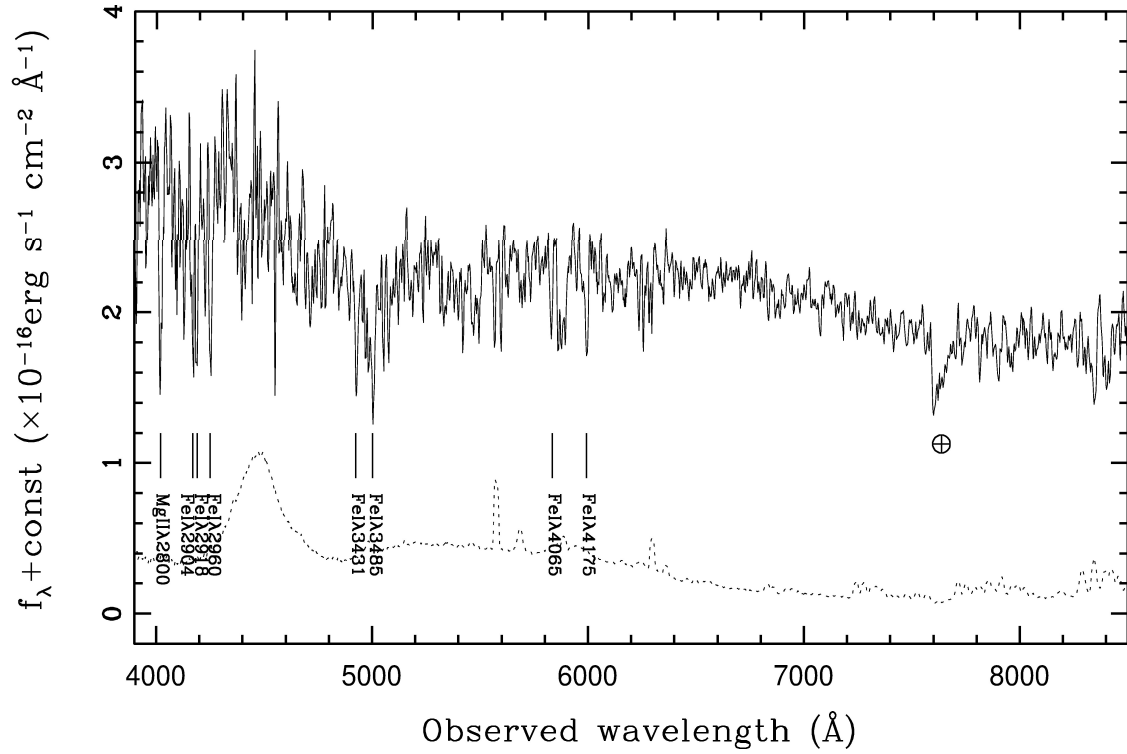


Figure 1. Optical spectrum (solid line) of GRB 210104A in the observer frame obtained with the Xinglong 2.16 m telescope at about 1 hr after the burst trigger. The spectrum is smoothed by a box size of 3Å. The night sky emission spectrum is shown as dashed line, and the identified absorption features both from the GRB afterglow and the strongest telluric feature at around λ 7600 are also marked.

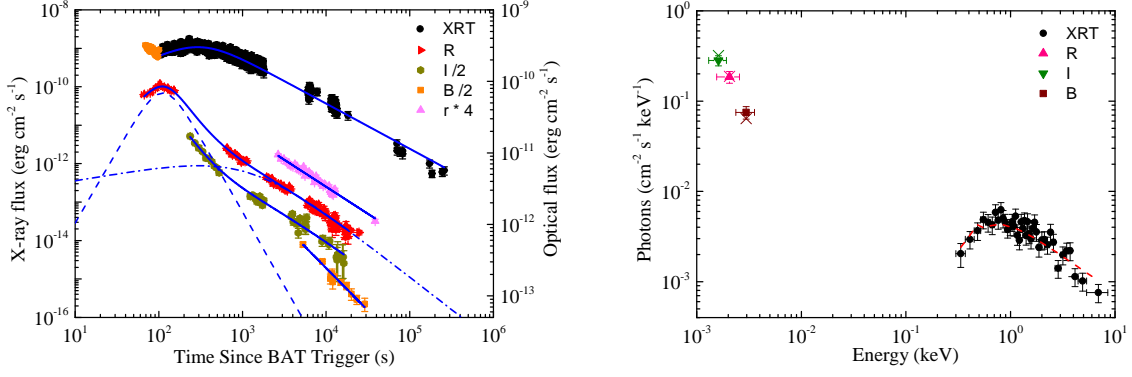


Figure 2. Left panel—Observed optical and X-ray afterglow lightcurves (data dots) of GRB 210104A together with our empirical fits (blue lines). Right panel—Joint optical-X-ray afterglow observed in the time interval of $[1.1 \sim 1.3] \times 10^4$ s of GRB 210104A along with our fit with a single power-law function (the red dashed line). The optical data are extinction-corrected for our Galaxy. Extinction and H I absorption of our Galaxy and the GRB host galaxy are considered in our spectral fit.

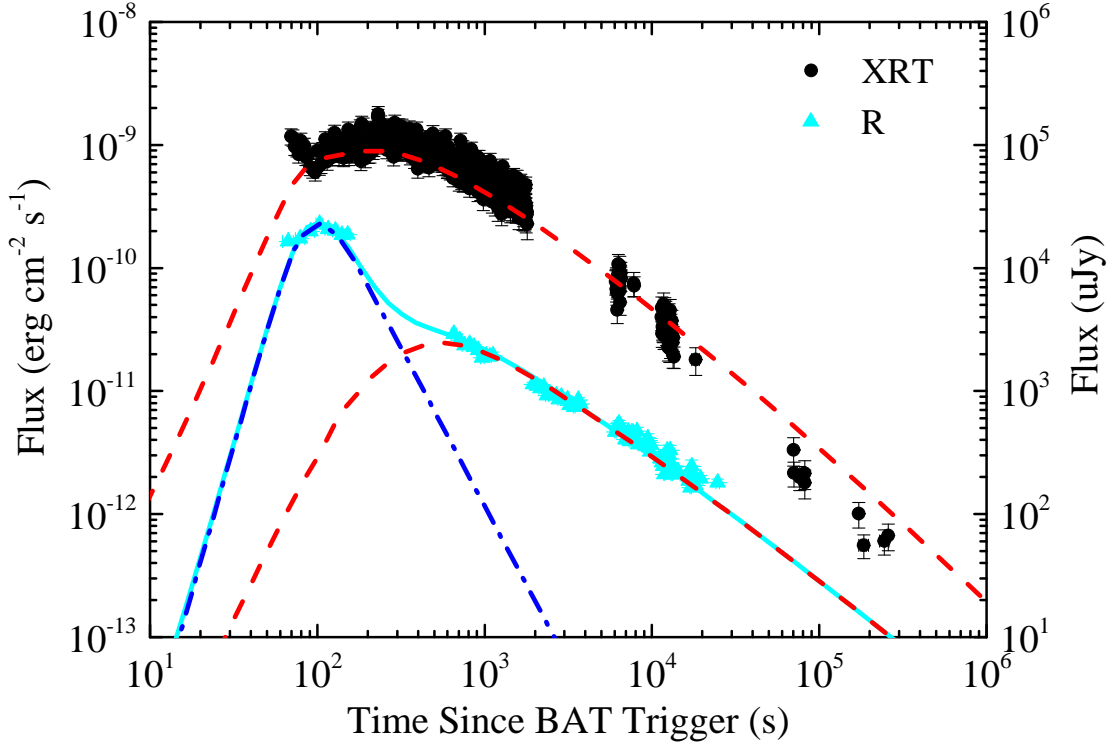


Figure 3. Our theoretical fit to the *R* band and X-ray afterglow lightcurves with the FS and RS models. The RS component is shown with a dashed-dotted line, and the FS component is shown with dashed lines.

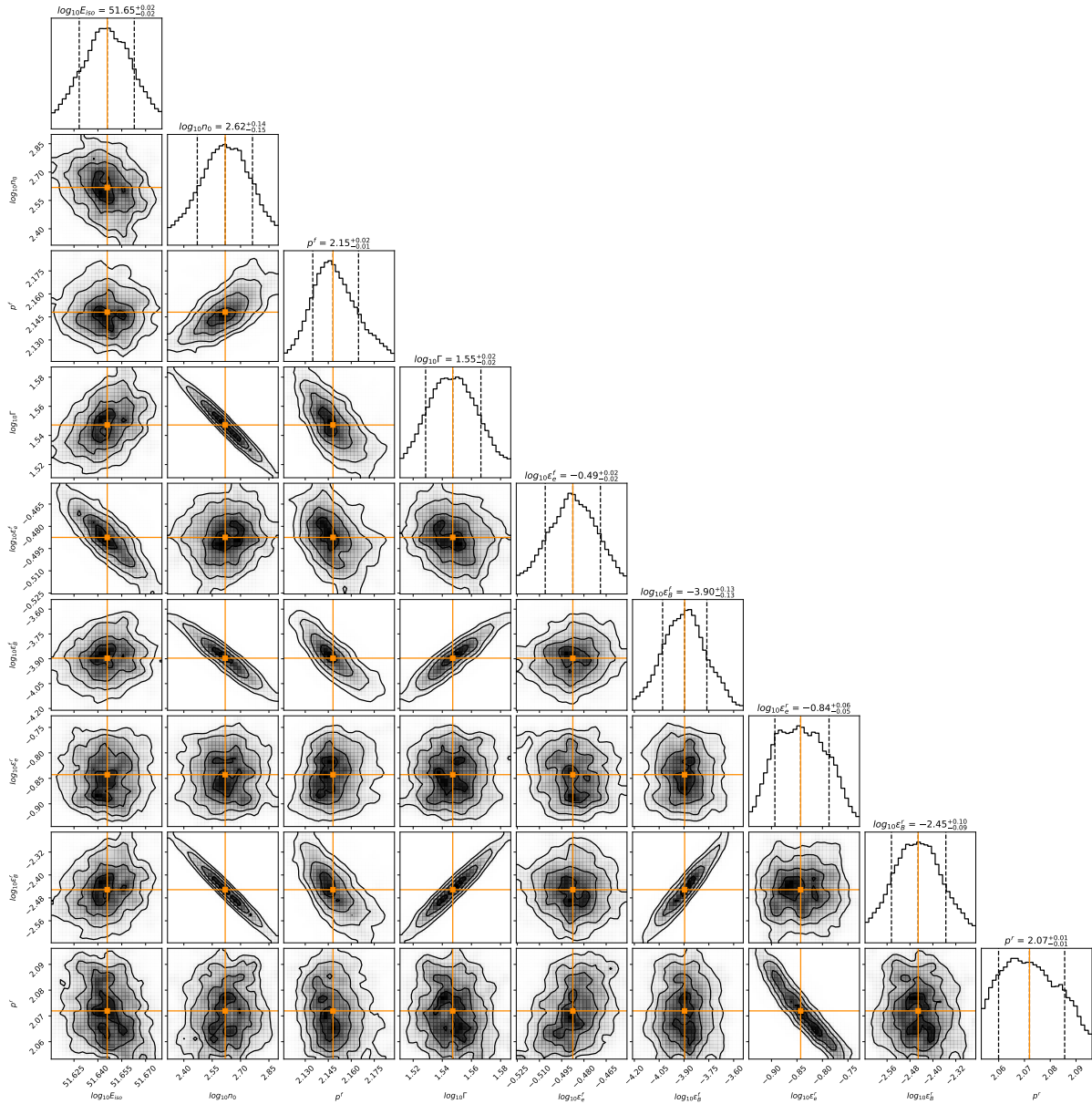


Figure 4. Corner plot of the one- and two-dimensional probability distributions of the model parameters derived from our fit to the R band and X-ray afterglow lightcurves of GRB 210104A with the MCMC algorithm. The 1σ regions centering at the median probability distributions are also reported in the tops and marked with vertical lines in each one-dimensional probability distributions.

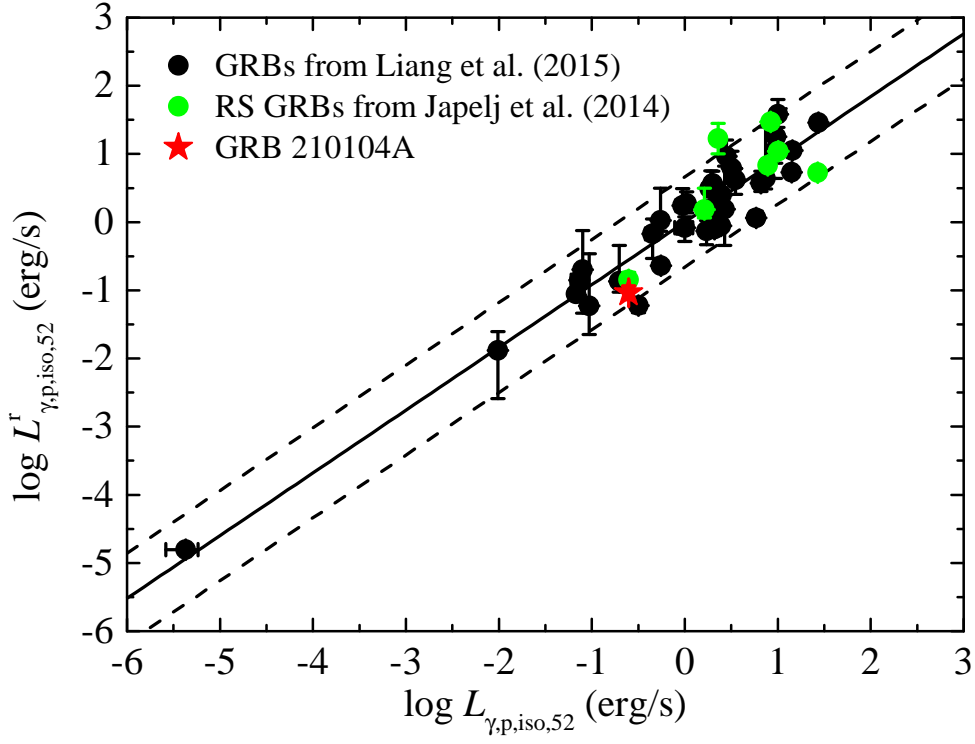


Figure 5. Luminosity calculated with the $L_{\gamma,iso} - E_{p,z} - \Gamma_0$ relation reported by Liang et al. (2015) as a function of the observed luminosity for GRB 210104A and other GRBs from Japelj et al. (2014) as marked in the plot. The solid and dashed lines mark the relation and its 2σ dispersion.